

# Curvature Analysis of Cardiac Excitation Wavefronts

A. Murthy<sup>1</sup>, E. Bartocci<sup>1,2</sup>, F.H. Fenton<sup>3</sup>, J. Glimm<sup>2</sup>, R. Gray<sup>4</sup>, S.A. Smolka<sup>1</sup>, and R. Grosu<sup>1</sup>

<sup>1</sup>Department of Computer Science, Stony Brook University, Stony Brook, NY

<sup>2</sup>Department of Applied Mathematics and Statistics, Stony Brook University, Stony Brook, NY

<sup>3</sup>Department of Biomedical Sciences, Cornell University, Ithaca, NY

<sup>4</sup>U.S. Food and Drug Administration, Silver Spring, MD

## ABSTRACT

We present the *Spiral Classification Algorithm* (SCA), a fast and accurate algorithm for classifying electrical spiral waves and their associated breakup in cardiac tissues. The classification performed by SCA is an essential component of the detection and analysis of various cardiac arrhythmic disorders, including ventricular tachycardia and fibrillation. Given a digitized frame of a propagating wave, SCA constructs a highly accurate representation of the front and the back of the wave, piecewise interpolates this representation with cubic splines, and subjects the result to an accurate curvature analysis. This analysis is more comprehensive than methods based on spiral-tip tracking, as it considers the entire wave front and back. To increase the smoothness of the resulting symbolic representation, the SCA uses weighted overlapping of adjacent segments which increases the smoothness at join points. SCA has been applied to several representative types of spiral waves, and for each type, a distinct curvature evolution in time (signature) has been identified. Moreover, distinguished signatures have been also identified for spiral breakup. This represents a significant first step in automatically determining parameter ranges for which a computational cardiac-cell network accurately reproduces ventricular fibrillation. The connection between parameters and physiological entities would then lead to an understanding of the root cause of the disorder and enable the development of personalized treatment strategies.

## Categories and Subject Descriptors

J.3 [Life and Medical Sciences]: Biology and Genetics

## General Terms

Systems Biology, Atrial Fibrillation

## Keywords

Curvature, Bézier Curves, Cardiac Models, Symbolic Com-

Permission to make digital or hard copies of all or part of this work for personal or classroom use is granted without fee provided that copies are not made or distributed for profit or commercial advantage and that copies bear this notice and the full citation on the first page. To copy otherwise, to republish, to post on servers or to redistribute to lists, requires prior specific permission and/or a fee.

CMSB '11, September 21-23, 2011 Paris, FR

Copyright 2011 ACM 978-1-4503-0817-5/11/09 ...\$10.00.

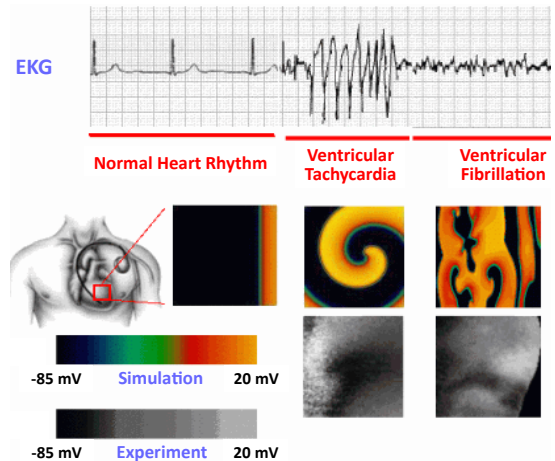


Figure 1: Emergent behavior in cardiac-cell networks. Top: Electrocardiogram. Middle and bottom: Simulation and experimental mappings of spiral waves of electrical activity occurring in the heart during tachycardia and fibrillation.

putation

## 1. INTRODUCTION

An estimated number of eighty one million American adults, that is more than one in three adults, have one or more types of cardiovascular disorders [11]. Among these disorders, ventricular tachycardia and especially fibrillation, may have devastating consequences (see Figure 1 and [6]).

Determining the physiological conditions responsible for a cardiac disorder is a grand challenge whose answer may lead to personalized treatment strategies. An important aid to this quest is the mathematical modeling, analysis and simulation of cardiac-cell networks [5]. Among the myriad of existing mathematical models, differential-equation models of reaction-diffusion type (DEMs) are arguably the most popular. In the context of DEMs the above challenge can be reformulated as follows: *For what parameter ranges does a DEM network accurately reproduce the cardiac disorder?*

The past two decades have witnessed the development of increasingly sophisticated DEMs [8], ranging from 4 to 67 state variables and from 27 to 94 parameters [4, 15, 19, 21, 10]. The increase in the number of state variables reflects the technological advances in capturing the intrinsic ionic mechanisms more accurately. The increase also leads

to a simplification of the differential equations. For example, most of the equations of the 67 variables DEM in [10] are of multi-affine type and were obtained using the law of mass action.

Unfortunately, the increase in the number of state variables, inevitably leads to an increase in simulation time. In particular, the simulation of the 67 variables DEM is so slow, that its authors only performed it in 1D (in a cable). In an accompanying paper, we present a CUDA-GPU implementation of the above-cited DEMs, on both Tesla and Fermi cards, with a dramatic reduction in simulation time. This allows us to perform for the first time on a desktop a 2D (on a surface) simulation of the 67 variables DEM.

Despite the difference in the number of state variables, the above DEMs are in some sense equivalent. Like in genetic regulatory networks (GRNs), the reduction in the number of variables can be understood as the result of a reaction (or time-scale) abstraction [18]. Akin to GRNs Michaelis-Menten or Hill-function abstractions, they reduce the number of state variables, at the expense of more complicated, sigmoidal dependencies among the remaining variables.

The lowest-dimensional DEM reproducing the experimentally macroscopic behavior of cardiac cells with great accuracy, is the 4 variables minimal model (MDM) of co-author Fenton [4]. The CUDA-GPU implementation of the MDM is so fast, that it allows the real time simulation of a  $500 \times 500$  grid of cells: One second of the MDM simulation time is approximately equal to one second of real time.

This increase in the MDM simulation speed, enables systematic exploration of its associated parameter space. For example, in a CMACS (Computational Modeling and Analysis of Complex Systems) workshop, organized this Spring at the Lehman College, we used ‘‘Crowd Sourcing’’ (CS), to explore pairs of parameter ranges that lead to fibrillation: Given a spiral-initiation protocol, the students were asked to simulate the MDM on each node of a 2D grid of parameter values, capture the generated waves and track the tip movement of their spirals. The results obtained, for example for MDM parameters  $\tau_w^-/\tau_w^+$ , are shown in Figure 2.

CS provided very encouraging initial results. However, CS is not likely to scale up to the exploration of parameter spaces involving more than two parameters. Such exploration requires at least two ingredients: 1) A principled way of partitioning the parameter space, and 2) A fast and accurate algorithm for classifying spiral waves and their breakup.

In a recent paper [9], we present a minimal hybrid-automaton (MHA) approximation of the MDM, which reproduces the MDM behavior with high accuracy. In each of its modes, the MHA is *multi-affine in the state variables* and *affine in the parameters* as per definition 1 of multi-affine functions in [3]. This allows a bifurcation analysis of the MHA which results in a partitioning of its parameter space into behaviorally-equivalent hypercubes. Each face (hyperplane) of the hypercubes separates the positive and negative ranges of the derivative of one of the MHA state variables. Hence, for simulation and analysis purpose, it is enough to select one parameter vector from each hypercube.

In this paper we present a fast and accurate algorithm (SCA) for classifying spiral waves and their associated breakup. Given a digitized frame of a propagating wave, the SCA constructs a highly accurate representation of the front and the back of the wave, piecewise interpolates this representation with cubic splines, and subjects the result to an accurate cur-

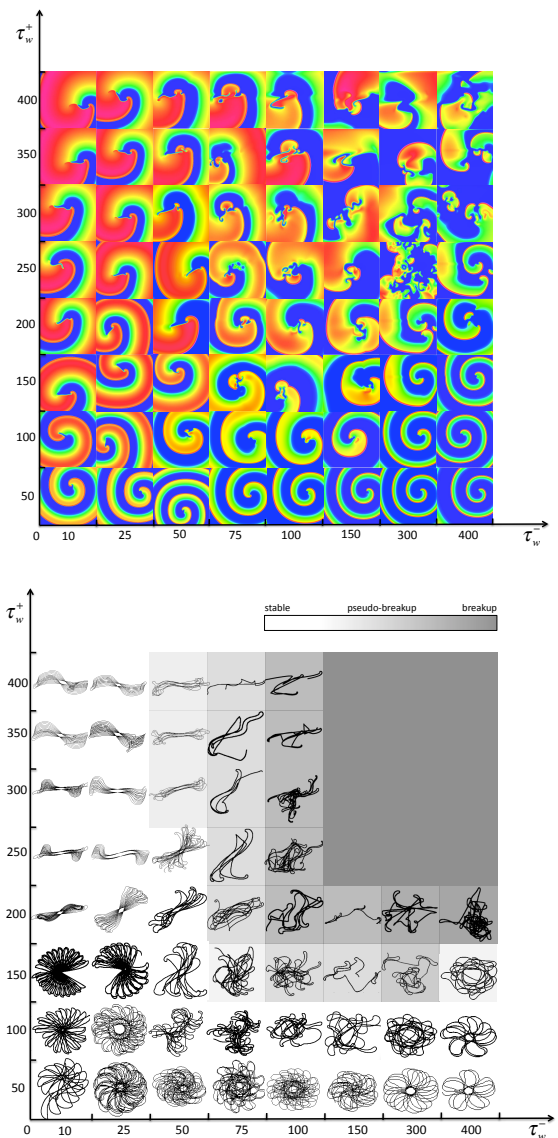


**Figure 2: Parameters  $\tau_w^-/\tau_w^+$ : (a) Wave forms. (b) Tip movement and regions of fibrillation.**

vature analysis. This analysis is more comprehensive than spiral-tip tracking, as it considers the entire front and back of a wave. To increase the smoothness of the resulting symbolic representation, the SCA uses a weighted overlapping of adjacent segments which increases the smoothness at join points. To speed up the SCA computation time, we employ a GPU-CUDA implementation. The SCA has been applied to several representative types of spiral waves generated with the MDM, and for each type a distinct curvature evolution in time (signature) has been identified. Moreover, distinguished signatures have been also identified for spiral breakup. This gives us hope that a *fully automatic answer to the grand challenge stated at the beginning of this section is within reach*: For what parameter ranges does an MDM network accurately reproduce ventricular fibrillation? Using the connection between parameters and physiological entities would then allow to understand the root cause of the

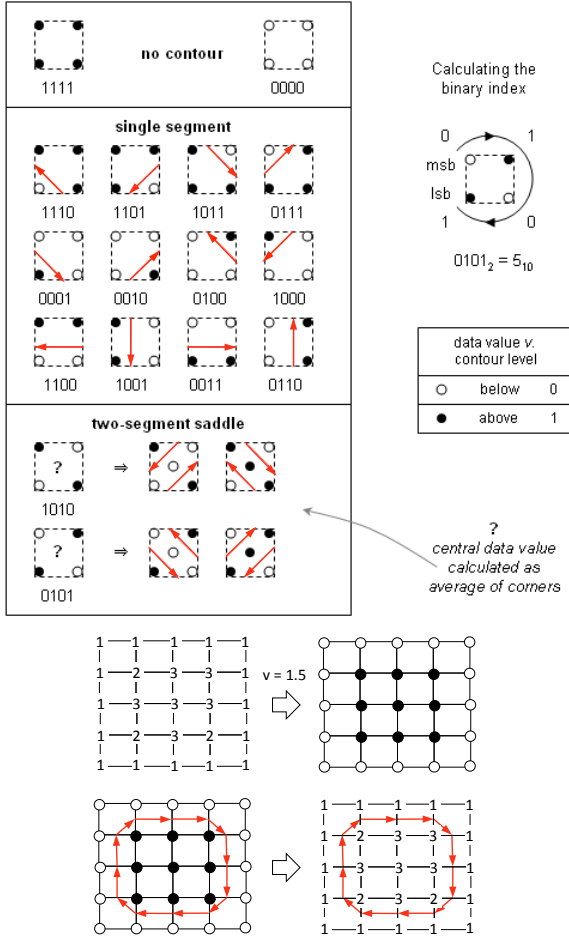


Figure 3: Marching squares.

disorder and develop personalized treatment strategies.

The rest of the paper is organized as follows. In Section 2 we discuss how to obtain the wavefront from a digitized frame. Section 3 discusses isopotential curvature estimation. Section 4 discusses our Bézier fitting algorithm which is improved in Section 5. Section 6 explains the symbolic evaluation of the curvature along the isopotentials. Finally, Section 7 discusses our case studies and directions of future work.

## 2. ISOPOTENTIAL RECONSTRUCTION

The simulation data obtained by executing an  $N \times N$  grid of MHAs, or the experimental data obtained by optically mapping a cardiac tissue, with resolution  $N \times N$ , is a sequence of *digital frames*  $F_t$  of dimension  $N \times N$ . Each frame  $F_t$  is the snapshot at time  $t$ , with resolution  $N \times N$ , of the trans-membrane *electrical potential*  $V_t$ , of the cardiac tissue.

The *wave-fronts* (*wave-backs*) of  $V_t$ , are the regions of  $V_t$  where each cell is in the activation (recovery) phase, that is their electrical potential  $V_t(x, y)$  equals  $-30\text{mV}$ , and their derivative  $dV(x, y)/dt$  is positive (negative). The two fronts define together the *isopotentials*  $I_{-30}$  of  $V_t$ . These are curves of constant voltage in  $V_t$ , that never intersect each other. For simplicity, when there is no danger of confusion, we will subsequently drop the subscript  $t$  occurring in  $F_t$  and  $V_t$ .

For any value  $v$ , the isopotentials  $I_v$  of  $V$  are smooth curves, whereas the isopotentials  $I_v$  of  $F$  are not. This is a consequence of the  $N \times N$  resolution. The *isopotential reconstruction problem (IRP)* is therefore defined as follows: *Given a frame  $F$ , and a voltage value  $v$ , reconstruct the smooth  $I_v$  isopotentials of  $V$ .* As we will see in the following sections, smoothness is essential for an accurate *curvature analysis (CA)* of the wave-fronts and wave-backs. The IRP remains the same when  $V$  is generalized to an arbitrary scalar field.

The *isopotentials reconstruction algorithm (IRA)* is the key component of SCA, as it consumes most of the memory and time resources of the SCA. Hence, IRA has to be designed very carefully, and run on an appropriate hardware platform, to make the SCA a success. Today, the CUDA-GPUs of the NVIDIA's Fermi or Tesla video cards, are an amazing such platform, which allows one to run a supercomputer on one's own desktop. We take advantage of these cards to implement a new *parallel, CUDA-based IRA (PIRA)*. To the best of our knowledge, this is the first algorithm of this kind.

PIRA belongs to a new CUDA based class of algorithms, which minimize the amount of synchronization; they require to reconstruct global information from a frame  $F$ . To achieve this goal, it divides its work in three parts: PMS) A fully parallel, local-information-computation procedure; PIE) A hierarchically parallel, global-information-computation procedure; and SOG) An optional, sequential to random-access, global-information-computation procedure.

### Parallel marching squares (PMS).

The fully parallel, local-information-computation procedure PMS uses an adaptation of the *marching squares* algorithm. Given a frame  $F$ , PMS considers in parallel, that is in a different thread of a CUDA block, each  $2 \times 2$  square  $s$ , of an adjacency-based  $(N-1) \times (N-1)$  partition of  $F$ . Each thread, locally and accurately computes the intersection points of zero, one or two lines, with  $s$ . The number of lines and their crossing pattern with  $s$  depends on the values in the corners of  $s$  (type of  $s$ ).

To determine the type of each square  $s$  of  $F$ , frame  $F$  is first subjected, in parallel, to the test  $F_{i,j} \geq v$ , for each index  $(i, j)$ . The result of the test is stored in a boolean matrix  $B$ . The boolean value of the corners of  $s$  in  $B$ , traversed say in clockwise order, determine 16 possible intersection cases. These cases are shown in Figure 3. In summary: 1) If all corners of  $s$  in  $B$  have the same value, there is no line crossing at all. 2) Otherwise, if diagonal corners have the same value, there are two ambiguous line crossings. Ambiguity is removed by averaging the value in all corners in  $s$  and comparing it with  $v$ . 3) Otherwise precisely one line is crossing  $s$ . Our adaptation, also associates each line a direction, by requiring that the 0 corners of square  $s$  only occur to its left.

An isoline intersects  $s$  only between two corners that have opposite boolean value in  $B$ . In other words, one corner has a value less than  $v$  and the other has a value which is greater than  $v$ . The intersection points, which also represent the starting and the ending points of a directed, one-segment-long polyline, are computed via linear interpolation. For example, suppose that the corners of  $s$  at position  $(i, j)$  in  $B$ , result in bitvector 0111. Then, the line segment crossing

$s$  has the points  $((x_0, y_0), (x_1, y_1))$  defined as follows:

$$\begin{aligned} x_0 &= j, & y_0 &= i + (v - F_{i,j}) / (F_{i+1,j} - F_{i,j}) \\ x_1 &= i, & y_1 &= j + (v - F_{i,j}) / (F_{i,j+1} - F_{i,j}) \end{aligned}$$

This information is stored in the corresponding one segment-polyline at position  $(i, j)$ , in an  $N \times N$  matrix  $S$  of squares. The starting and ending polylines of the open polylines list are initialized to the location of this polyline. If there are two polylines, the first one is the first in the list and the second one, the second. The list of closed polylines is initialized to null. The number of polyline segments and the number of open/closed polylines is also appropriately initialized.

```

struct Point // typed points
{
    int type; // 0 = row crossing, 1 column crossing
    float x,y; // x and y coordinates
    float y; // y coordinate
}
struct PolyLine // directed polylines
{
    int type; // 17 types
    int number; // number of segments
    Point start, end; // start and end points
    PolyLine * next; // ptr to next polyline
}

```

To speedup the interpolation process, the case analysis of the square type is efficiently pre-stored in a lookup table  $T$ , allocated in the constant memory of the GPU card.

```

struct Square // Data Structure for Squares
{
    int num_of_opl; // number of open polylines
    int num_of_cpl; // number of closed polylines
    PolyLine * opl_start; // pointer to first open polyline
    PolyLine * opl_end; // ptr to the last open polyline
    PolyLine * cpl_start; // ptr to the first closed polyline
    PolyLine * cpl_end; // ptr to the last closed polyline
    PolyLine poly_lines[2]; // storage allocated on leaf level
}

```

For each square type  $t$  and for each one-segment polyline  $p$ , the table consists of the following entries: Two line coefficients and four coordinate displacements. For the above example, where  $t = 7$ ,  $p = 0$ , table  $T_{t,p}$  contains:

$$T_{t,p} = \{ \{ a = 0, b = 0, i_1 = 0, j_1 = 0, i_0 = 0, j_0 = 0 \}, \\ \{ a = 1, b = 0, i_1 = 1, j_1 = 0, i_0 = 0, j_0 = 0 \}, \\ \{ a = 1, b = 0, i_1 = 0, j_1 = 1, i_0 = 0, j_0 = 0 \}, \\ \{ a = 0, b = 0, i_1 = 0, j_1 = 0, i_0 = 0, j_0 = 0 \} \}$$

Denote  $T_{t,0}$  and  $T_{t,1}$  with the corresponding field names, indexed by subscripts 0 and 1. Then the one-segment-polyline starting coordinate can be computed uniformly, as follows:

$$\begin{aligned} x_0 &= j + b_0 + a_0(v - F_{i+i_{00},j+j_{00}}) / (F_{i+i_{01},j+j_{01}} - F_{i+i_{00},j+j_{00}}) \\ y_0 &= i + b_1 + a_1(v - F_{i+i_{10},j+j_{10}}) / (F_{i+i_{11},j+j_{11}} - F_{i+i_{10},j+j_{10}}) \end{aligned}$$

### Parallel isoline extraction (PIE).

Using PMS one can readily plot the isolines of  $V$ . However, there is no global information available yet, despite of the fact that we know the isoline segments, their orientation, and their linking. However, we do not know: 1) What is the belonging of segments to particular isolines? 2) How many isolines are in  $V$ ? 3) How many segments they contain? and 4) What is their starting and ending point. It is only our brain that connects segments in a meaningful way.

The public `contour` function of Octave uses a sequential, recursive algorithm, to obtain global information. This works as follows: 1) Traverse a matrix of interpolated segments, row by row and column by column, and pick the first

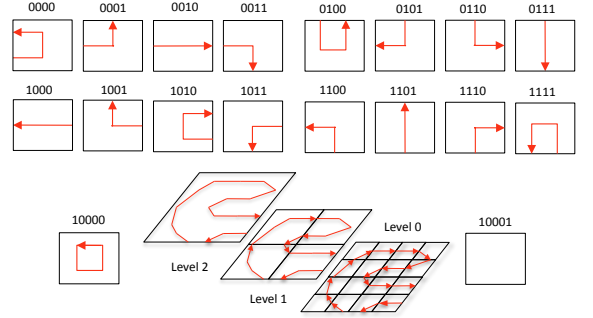


Figure 4: Isopotential extraction.

unmarked one. 2) Then recursively follow matching segments in a meaningful way, until the border or the starting point is reached again (no direction is readily available as in our PMS). During this process, dump all points traversed in a dynamic array, and mark all the segments as visited. 3) Once an entire isoline is found, search for the next unmarked segment, until the last row and column is reached.

Recursion and the sequential traversal of the entire matrix of segments is however prohibitive, for a fast curvature analysis. The `isoline` function available at [17], is sequential, but not recursive. It: 1) Uses the marching squares algorithm to compute all (disoriented) segments and dump them, in no particular order, in a dynamically allocated array. 2) Then, it extracts the first unmarked segment, and repeatedly searches the entire array for an unmarked, matching continuation. Its time complexity is therefore, comparable with the one of the recursive algorithm.

To obtain a fast algorithm, we take advantage of the GPU cards. This imposes however, several important restrictions on PIE: 1) It cannot be recursive; 2) It cannot dynamically allocate memory; 3) It can only contain for-loops, with known upper bound. As shown in Figure 4, the main idea of PIE is to organize the squares  $S$  passed by PMS, in a quad-tree fashion, such that, at every level in the tree hierarchy, sibling nodes (and their immediate children) are processed in parallel, by a different CUDA thread. Hence, global information is computed sequentially, in  $\log_4 N$  steps.

During this process, a parent either collects or pastes together the polylines of its children, if they have matching start and end points. A particular problem during this process is dynamic memory allocation. In the CUDA core, such allocation is not possible. Moreover, there is no way to predict in advance, without gross overestimation, the amount of memory needed in each node, to store the list of polylines it has identified so far, and the polylines themselves.

Our solution is to reuse the memory already allocated in the leaf squares, for their two one-segment-long polylines, during the upward sweep of the quad-tree. Each time, when information is collected from the 4 children, the result is stored in child 0. This information is later on passed upward in the hierarchy. Child 0's information gets therefore lost.

Whenever the parent process matches the ending point of polyline  $p$  of child  $c$ , with the starting point of polyline  $q$  of child  $d$ , it updates the starting and end points of polyline  $pq$  in  $p$ , and removes  $q$  from the polyline list of child  $d$ . It then continues from a copy of  $q$  to find the next match. The total number of matches, is bound by the number of polylines in all children, and this is used in a find-next-match for-loop. This loop is the equivalent of the recursive match-next-segment search in `contour` or `isoline`, but it is limited

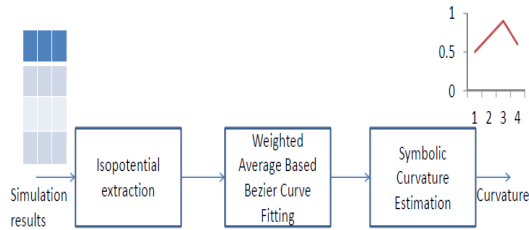


Figure 5: Block diagram for curvature estimation

to the *polylines* of the parent’s children. This dramatically decreases the time complexity of the recursive search.

Whenever, the parent process collects the polyline lists of the children, it appends these lists to the lists of child 0. For this purpose, the Square structure has the start/end fields of the list of open/closed polylines, and each polyline has a next polyline field. The number of polylines, and the number of segments, are also updated accordingly.

In order to efficiently match the end point of a polyline  $p$  of a child  $c$  with the starting point of a polyline  $q$ , it is important to know what sibling of  $c$  might have such a  $q$ . For this purpose, we classify the polylines according to their starting and ending faces in  $c$ , as shown in Figure 4. This leads to a classification of polylines, that is similar to the one for squares. In contrast to squares however, polylines may start and end up on the same face, or they may be closed, that is, they are completely contained in  $c$ . The second case does not require further processing. Similarly, if a polyline of square  $c$ , starts and ends on a face that is not adjacent to any of the  $c$ ’s siblings, no processing is required at this level either. To enable this kind of analysis, a type field is added to the polyline data structure, too.

and propagating information, is that the linking information of one-segment-long polylines is lost. Consequently, one has to store this information in a different place. For simplicity and speedup reasons, we allocate two hash tables  $X$  and  $Y$  of size  $N \times N$ : the first is indexed by the integer value of horizontal intersection points, the second by the integer value of vertical intersection points. Each entry of  $X$  and  $Y$  stores the destination point and a bit classifying it as a horizontal or vertical intersection. This allows to determine whether to choose the  $X$  or the  $Y$  hash table next. In general, unless the isolines are fractals, the number of segments is orders of magnitude smaller than  $N \times N$ . Hence, more information acquired about the kind of isolines to expect, may improve the size allocation, by choosing an  $M \ll N$  for these tables.

#### Output generation procedure (SOG).

The optional SOG procedure selects the isolines of interest according to some given criterion, for example the longest isoline, and stores the points of these isolines in an array, sorted by their traversal order. The size of the isolines, their starting point, and their ending point are available at the root of the quad tree. This information is used to dynamically allocate the corresponding arrays, outside of the CUDA core. The  $X$  and  $Y$  hash tables are then used to traverse the associated isoline and dump the points traversed in the array. This process transforms the local, sequential-linking information, in a global, random-access information, where entry  $i+1$  is known to be the successor point of entry  $i$ .

We have reconstructed the isolines of 10 000 frames, both with PIRA and the *contour function* of Matlab. The first took 1.65 seconds while the second took 720 seconds. Hence, PIRA had a 444.444 fold speedup compared to *contour*. The rest of SCA has not been parallelized yet. However, this is easily accomplished as we describe in the next sections.

### 3. CURVATURE ESTIMATION

Propagation patterns of cardiac waves (isopotentials produced by SOG in the previous section) characterize cardiac arrhythmia. Obstacles or deformities affect the linear motion of cardiac waves resulting in anomalous propagation. Re-entry is one such abnormal movement in which cardiac waves assume spiral paths that are precursors to more dangerous fatal arrhythmia. When these spiral waves break up, fibrillation a possibly fatal arrhythmia follows. [14] points to experimental evidence that shows atrial fibrillation is characterized by re-entrant cardiac waves that break up and exhibit chaotic patterns.

Local geometric features like curvature can be a critical in affecting wave propagation and breakups. [7] establishes the relation between the curvature of the isopotential and its propagation velocity. If  $\theta_0$  is the steady state velocity of a linear isopotential then the velocity of a curved one is given by  $\theta = \theta_0 - \frac{D}{r}$  where  $r$  is the local radius of curvature and  $D$  is a co-efficient determined by passive properties of cardiac medium. Thus any part of the isopotential that has high positive curvature slows down and eventually breaks off. Also, the existing arrhythmia can be classified accurately based on curvature of the underlying cardiac waves. An efficient way of measuring curvature will thus be very helpful in predicting and identifying arrhythmia.

Any method that estimates curvature of cardiac isopotentials must satisfy two requirements: 1.) The technique must be accurate. 2.) The method employed must provide curvature values continuously along the perimeter of the isopotential. Thus the method must be independent of the spatial resolution at which the isopotential is estimated or the grid on which the cardiac model is solved.

Our technique of curvature estimation can be represented by the block diagram of figure 5. The isopotential obtained in the previous section is a series of points on  $\mathbb{R}^2$ . Starting from this, our method of obtaining a smooth curvature estimate involves the following steps:

1. **Step 0 - Preprocessing:** Divides the isopotential obtained by SOG into overlapping strips of constant length.
2. **Step 1 - Bézier curve fitting:** Fits each strip with a third degree Bézier curve, thus obtaining a piecewise degree-3 polynomial fit of overlapping Bézier curves.
3. **Step 2 - Estimate curvature using symbolic analysis:** Curvature is calculated along the Bézier curves using symbolic calculations.
4. **Step 3 - Obtain overall curvature estimate:** Obtains a smooth estimate of curvature along the entire isopotential.

First, we divide the isopotential  $I_v$  into overlapping segments that we call *strips*. The length of each strip is controlled by the parameter STRIP\_LENGTH (SL). The percentage overlap among them is controlled by OVERLAP.

This is the initial pre-processing done before polynomial fitting. The following sections describe each of the remaining steps in detail.

#### 4. PIECEWISE BÉZIER FITTING

Most of the formalisms of curvature in  $\mathbb{R}^2$  involve second order derivative terms. This motivates a need to obtain at least a degree-3 polynomial approximation to the Isopotential. We fit the isopotential with overlapping cubic Bézier curves in a piece-wise manner, thus satisfying the above requirements of curvature estimation.

Given a strip  $I_{v,j}$ , we want to obtain one Bézier curve that approximates this strip up to a certain degree of L2 error. A Bézier curve approximation for  $I_{v,j}$  would have the form below where  $t \in [0, 1]$ :

$$X_j(t) = (1-t)^3 P_j^0 + 3t(1-t)^2 P_j^1 + 3t^2(1-t) P_j^2 + t^3 P_j^3 \quad (1)$$

$$Y_j(t) = (1-t)^3 Q_j^0 + 3t(1-t)^2 Q_j^1 + 3t^2(1-t) Q_j^2 + t^3 Q_j^3 \quad (2)$$

Here  $P_j^0 - P_j^3$  and  $Q_j^0 - Q_j^3$  are the control points of the Bézier curves that approximate the isopotential strip along  $X$  and  $Y$  axis respectively. To sample from this curve, we evaluate the above expressions over the interval  $t \in [0, 1]$ .  $P_j^0, P_j^3, Q_j^0$  and  $Q_j^3$  are the terminal control points which coincide with the data. The fitting procedure adapted from [13] and [20] optimizes the intermediate control points  $P_j^1, P_j^2, Q_j^1$  and  $Q_j^2$  to minimize the least squares error. We assume uniform parametrization of  $t$  in  $[0, 1]$  for each segment. Thus error functions while fitting  $I_{v,j}$  are:

$$E_x = \sum_{i=1}^{SL} [x_i - X_j(t_i)]^2, E_y = \sum_{i=1}^{SL} [y_i - Y_j(t_i)]^2$$

Replacing equations 1 and 2 in the above error functions respectively we obtain:

$$\sum_{i=1}^{SL} [x_i - (1-t_i)^3 P_j^0 + 3t_i(1-t_i)^2 P_j^1 + 3t_i^2(1-t_i) P_j^2 + t_i^3 P_j^3]^2,$$

$$\sum_{i=1}^{SL} [y_i - (1-t_i)^3 Q_j^0 + 3t_i(1-t_i)^2 Q_j^1 + 3t_i^2(1-t_i) Q_j^2 + t_i^3 Q_j^3]^2$$

as expressions for  $E_x$  and  $E_y$  respectively. The following calculations are shown only for  $E_x$ . For  $E_y$  the expressions follow from those for  $E_x$ .  $P_j^1$  and  $P_j^2$  can be obtained at the minimum value of  $E_x$  by

$$\frac{\partial E_x}{\partial P_j^1} = 0, \frac{\partial E_x}{\partial P_j^2} = 0$$

Solving the above two equations we obtain the following expressions for  $P_j^1$  and  $P_j^2$ :

$$P_j^1 = \frac{\alpha_2^j \beta_1^j - \alpha_3^j \beta_2^j}{\alpha_1^j \alpha_2^j - \alpha_3^j}, P_j^2 = \frac{\alpha_1^j \beta_2^j - \alpha_3^j \beta_1^j}{\alpha_1^j \alpha_2^j - \alpha_3^j}$$

where  $\alpha_1, \alpha_2, \alpha_3, \beta_1$  and  $\beta_2$  for each segment are given by:

$$\alpha_1 = 9 \sum_{i=1}^{SL} [t_i^2(1-t_i)^4]$$

$$\alpha_2 = 9 \sum_{i=1}^{SL} [t_i^4(1-t_i)^2], \alpha_3 = 9 \sum_{i=1}^{SL} [t_i^3(1-t_i)^3]$$

$$\beta_1 = 3 \sum_{i=1}^{SL} [t_i(x_i - (1-t_i)^3 P_0 - t_i^3 P_3)(1-t_i)^2]$$

$$\beta_2 = 3 \sum_{i=1}^{SL} [t_i^2(x_i - (1-t_i)^3 P_0 - t_i^3 P_3)(1-t_i)]$$

The above procedure explains how cubic Bézier curves are fit on one strip of the isopotential. To make the curvature estimates smooth, we fit the curves on overlapping segments.

#### 5. WEIGHTED AVERAGE BASED IMPROVEMENT

The fitting procedure described above is sequential in nature. However, for every strip selected, one can run this procedure in parallel, by using a different CUDA-thread on the GPU cards. Although we did not do this yet, this is a simple adaptation of this algorithm.

After each strip is fit with cubic Bézier curves as explained above, we improve the smoothness of the overall fit. A pure piece-wise fitting approach will create discontinuities in the derivative of the isopotential-approximation at the points where two curves meet. We ensure that derivatives up to second order are well defined everywhere on the isoline. To do this, fitting is performed on overlapping strips. Parameter OVERLAP determines the percentage overlap between adjacent strips of the isopotential.

Consider a part of the isopotential that has two adjacent overlapping strips with indices  $j$  and  $j+1$ . To define the Bézier curve fit for this part of the isoline, we use a weighted average based method. Suppose the curves describing the two strips are  $f_j$  and  $f_{j+1}$ , then the fit for the region covered by the two strips is given by  $w_j f_j(t_j) + w_{j+1} f_{j+1}(t_{j+1})$ , where  $w_{j+1} + w_j = 1$ . In essence, the influence of the adjacent curves on the fit is gradually varied in the region of overlap. In the region where there is no overlap, the fit is completely described by the only Bézier curve corresponding to that strip. As one enters the region of overlap, the fit is a weighted average of the two Bézier curves corresponding to adjacent strips. The weights are varied linearly in our scheme as shown in figure 6. The same weighted average smoothing is performed for the derivatives and curvature values.

Each Bézier curve is a third degree polynomial. In the overlapping region, the fit is a weighted average of two cubic polynomial functions. Thus even in the overlapping region the fit is  $C^2$  smooth rendering it amenable to curvature estimation described in next section. The smoothing described above can also be performed in parallel. This weighted average based scheme helps us obtain smooth polynomial approximation of the complete isopotential. This is different from [12] which uses cubic splines to fit the isopotentials.

#### 6. CURVATURE ESTIMATION USING MATLAB SYMBOLIC COMPUTATION

We use symbolic computations in MATLAB to evaluate curvature along the isopotential. This constitutes step 2 of our method listed above. The fitting procedure described

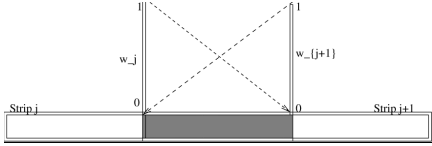


**Figure 6: Weighted average based fit smoothing and curvature estimation**

above provides smooth Bézier curves that describe the isopotentials. As these are closed form expressions, they can be manipulated symbolically. MATLAB’s symbolic toolbox provides the facility to declare symbolic variables, construct functions out of them and operate on those functions. Once the operations yield the expressions of interest, they can be evaluated at arbitrary resolution by suitably specifying the interval for the symbolic variables.

In our case, we obtain the functions  $X_j(t)$  and  $Y_j(t)$  for each strip. The curvature of this strip of the isopotential is derived using elementary calculus:

$$\kappa_j(t) = \frac{|r'_j(t) \times r''_j(t)|}{|r'_j(t)|^3} \quad (3)$$

where  $r_j(t) = [X_j(t), Y_j(t)]$  is the position vector described by the Bézier curve.

The important point to note is that  $X_j(t)$ ,  $Y_j(t)$  and thus  $r_j(t)$  are managed as symbolic expressions which are functions of the symbolic variable  $t$ . Thus  $\kappa_j(t)$  is obtained in closed form as an expression in  $t$ . Symbolic operations on  $r_j(t)$  is performed using MATLAB’s symbolic math toolbox. [16]

After obtaining closed form expressions for curvature, their continuity ensures that we can evaluate them at any resolution of the parameter  $t$ . This translates to obtaining continuous estimate of curvature along the perimeter of the isopotential.

Step 3 of our method evaluates these curvature functions along the isopotential using the weighted approach technique described in the previous section. Currently we maintain uniform resolution for  $t$  along all the strips. Adapting this to the shape of the isoline is part of our future work. In particular, the information stored in the quad-tree of PIE, for example the filling factor of the area associated to its nodes might facilitate a fast and accurate breakup of the isoline in isoline-strips, improving on the idea in [12].

The runtime for curve fitting and curvature calculation routines depend on the length of the Isopotential. Extraction process checks each grid square for a possible point of the isopotential. The number of edges on a  $n \times n$  grid can be calculated by solving the following recurrence:

$$E(n) = E(n-2) + 4n + 4(n-3) + 8 \quad E(1) = 4, \quad E(2) = 8 \quad (4)$$

The solution is given by

$$E(n) = -2(-1)^n + 2n(n+1) - 2 \quad (5)$$

Hence the maximum length of the isoline is  $O(n^2)$ , which bounds the number of operations in the fitting and curvature routines to  $O(n^2)$ .

## 7. CASE STUDIES

To demonstrate our isopotential tracking and curvature estimation techniques, we simulate four different forms of cardiac arrhythmia. On the simulation results we apply isopotential extraction on each frame. Then we estimate the curvature along the cardiac wave to capture the characteristic trend in time for that particular arrhythmia. In the following sub-section we show for each case study: 1.) one typical frame from simulation results 2.) isopotential that was tracked 3.) weighted average based Bézier curve fit and 4.) curvature trend in time for that simulation. It should be noted that to generate 4.) we plot the closed form functions corresponding to curvature. The function itself can be evaluated at any resolution of the Bézier curve parameter  $t$ .

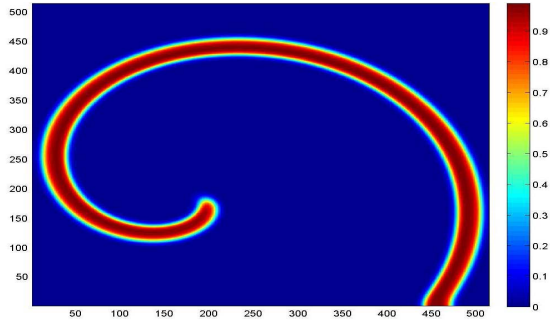
The purpose of these case studies is two-fold. Firstly we demonstrate the correctness of isopotential extraction and curvature estimation techniques explained above. Also the results show the feasibility of using curvature trend as a feature to classify different arrhythmic spiral excitation waves. The case studies were generated such that the tip of the spiral traces trajectories of different shapes resulting different types of abnormal propagation.

*1: Re-entry with circular core:* Re-entrant spiral waves in atrial chambers are precursors to ischemic stroke and fibrillation. In this case study we simulated the Barkley model [1] on a tissue of  $514 \times 514$  cells. Time scale used was 10ms. The core of the spiral shaped excitation waves traced a circular trajectory. One sample frame of simulation result is shown in figure 7(a). After initial excitation, the spiral shaped isopotentials were extracted at a scaled level of 0.7.

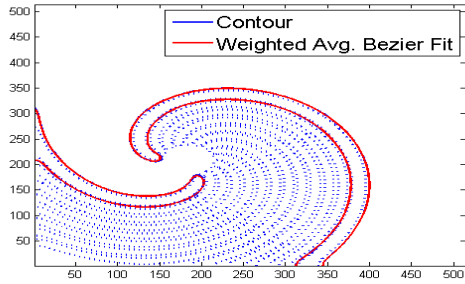
Figure 7(b) shows the propagation of isopotential with the tip tracking a circular trajectory. The wave in the first and last time step of simulation is shown in solid blue. The overlapping red curve is the weighted average based Bézier fit. Isopotentials are shown for intermediate frames in dotted blue. As the spiral rotates, its tip tracing a circular trajectory, the basic shape of the wave remains unchanged. As the basic shape of the wave remains unchanged, we would expect the curvature trend to remain the same over time. The curvature trend is shown in figure 7(c). The region of maximum curvature corresponds to the spiral tip which remains around the center of the isopotential throughout the simulation. The rest of the isopotential shows a relatively lower curvature. This trend characterizes spiral reentrant waves in the heart.

*2: Re-entry with Hypocycloidal core:* It is not always the case that the tip is located around the center of the spiral wave. To simulate asymmetric shapes, we generated waves whose tip traces hypocycloidal trajectories. In this case study, a tissue of size  $1024 \times 1024$  was simulated using the minimal model [4]. The isopotential was extracted again for 0.7 and the time scale of the simulation was 10ms. A typical frame of the simulation can be seen in figure 8(a). Both the isopotential extracted and the Bézier fit is shown for the first and last frame of the simulation. The intermediate dotted blue lines are isopotentials for some of the intermediate frames.

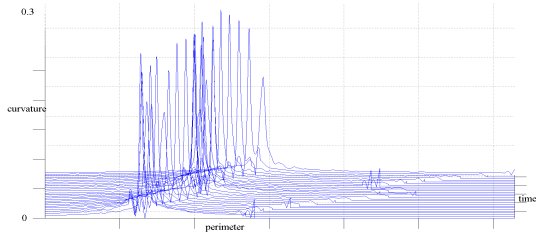
As the tip rotates, the length of the wave changes and at times, the tip is not the center of the isopotential. This turning causes the shape of the wave to become asymmetric. The turn of the spiral is evident in the curvature trend in figure 8(c). As the length of the spiral changes, the region of highest curvature shifts on the curvature trend. This



(a) Numerical Simulation



(b) Isopotential evolution



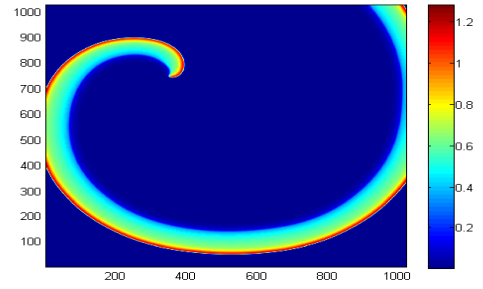
(c) Curvature Trend

**Figure 7: Results for case study 1: Re-entry with circular core**

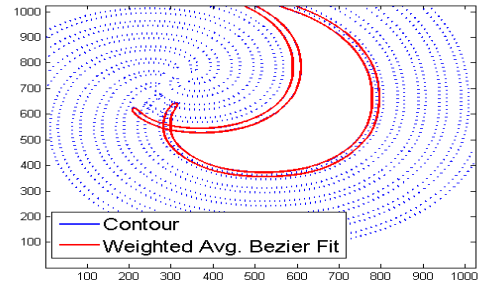
further demonstrates that a trend of morphological features like curvature, can capture the dynamics of different cardiac arrhythmia.

*3: Re-entry with Linear Core:* In practice spiral waves may exhibit more complex behavior. In the presence of an obstacle or deformity in the medium, waves rotate while traversing linear trajectories. For this case study, a tissue of  $1024 \times 1024$  cells was simulated under the minimal model [4] at a time scale of 10ms to produce this behavior. Isopotential extraction was done for a scaled level of 1.0. Figure 9(a) shows a snapshot of the simulation. The linear trajectory along which the wave rotates can be seen with the tip of the wave at one end. Figure 9(b) shows the evolving isopotential. It starts out from the solid isopotential line near the top of figure 9(b) and ends at the solid isoline in the lower half.

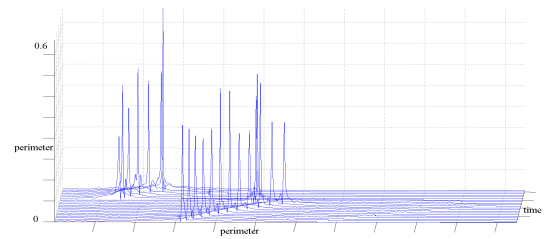
During its linear motion, the wave has three regions of high curvature. The first two are present at the ends of



(a) Numerical Simulation



(b) Isopotential evolution



(c) Curvature Trend

**Figure 8: Results for case study 2: Re-entry with hypocycloidal core**

the linear path of the tip. As always, the highest curvature is found at the tip which separates the wavefront and the wave-back. As the tip moves along the linear path, the separation between curvature peaks corresponding to the high curvature regions, changes. The highest peak starts near the left peak that corresponds to the first high curvature bend of the isopotential. With time, as the tip moves down to the other end of the linear path, the central curvature peak shifts toward the right peak.

Thus the presence of an obstacle or deformity is strongly correlated with the curvature trend shown in figure 9(c). Moreover, if the simulation is continued to run, the trend repeats itself which can further strengthen the classification.

*4: Spiral Wave Breakup:* We study the onset of fibrillation in this case study. The spatio-temporal definition of the fibrillating myocardium involves the break-up of re-entrant waves[14]. This break-up creates daughter spirals which interact to produce emergent behavior. Thus predicting the

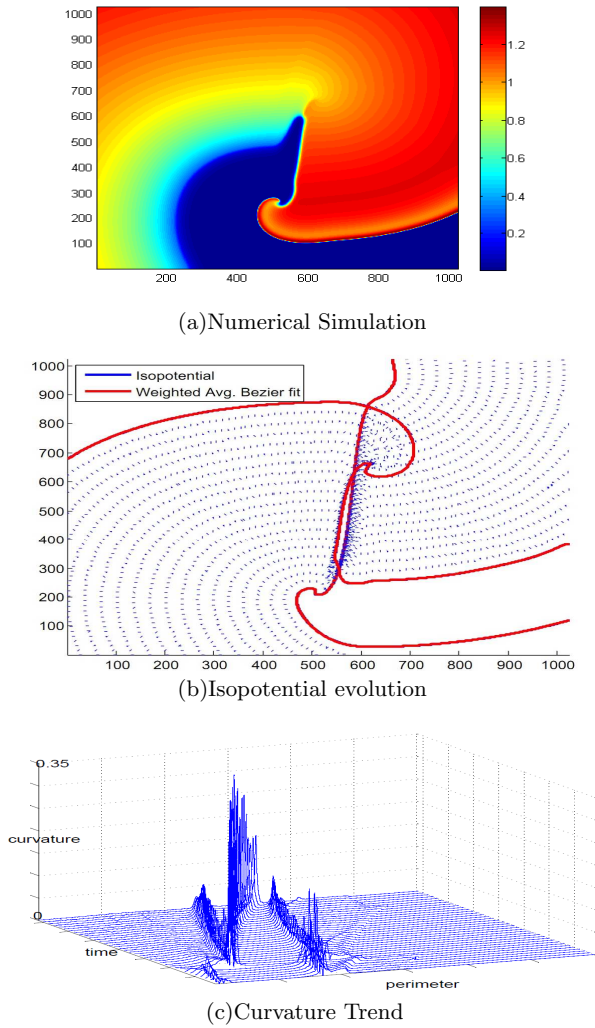


**Figure 9: Results for case study 3: Re-entry with linear core**

spiral break-up is crucial to the problem of predicting fibrillation. A tissue of  $1024 \times 1024$  cells was simulated using the Beeler-Reuter model[2]. Spiral break-ups occur at a very short time scale. The model was simulated at 1ms time scale to allow for detection of abrupt changes in isopotential morphology.

Figure 10(a) shows one simulation frame where the first break-up has already occurred. We track the isopotential of value 4.0 till the first break-up occurs. As we approach the moment of detachment, the isopotential shows a dent near the site of break-up. This change in shape translates to creation of a high curvature region. The changing shape of isopotential is shown in figure 10(b). Again, the isopotential and the polynomial fit is shown for the first and last step and intermediate steps are shown in dashed lines. As compared to other studies, there seem to be fewer intermediate curves. This is because, at a small time scale of 1ms, most of the frames do not show any change, leading to over-

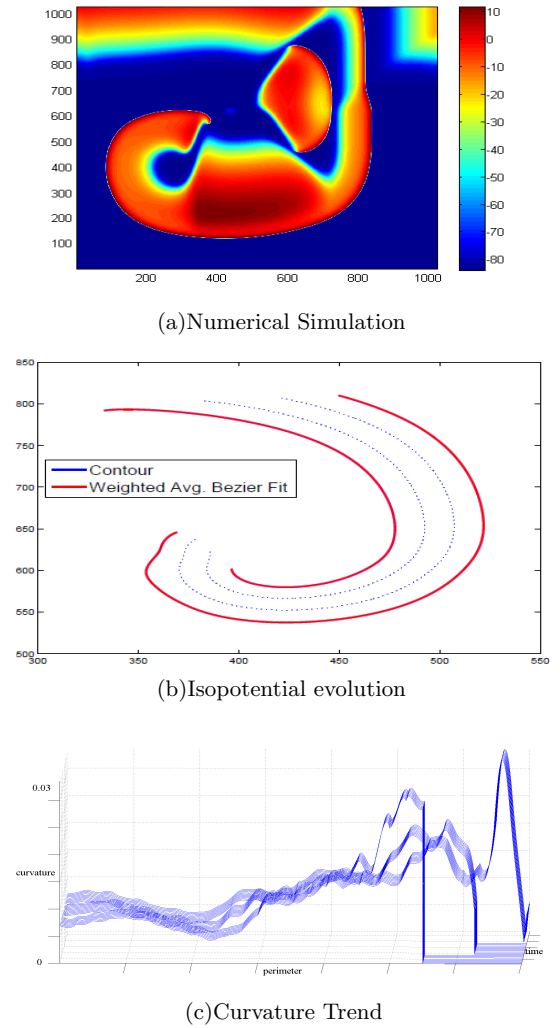


**Figure 10: Results for case study 4: Spiral break-up**

lapping isopotentials. The time scale at which detachment occurs forced us to lower the time scale to observe the trend in curvature.

Figure 10(c) shows the trend of curvature as the isopotential evolves toward breakup. Just before detachment, we see high curvature corresponding to the evolving site of break-up. Thus the gradual buildup of a high curvature site on the wave is a strong indication of future break up leading to eventual fibrillation.

## 8. CONCLUSION

The technological developments within the graphical processors community, NVIDIA in particular, coupled with the theoretical advances in the computer-aided verification community, have set the stage for fast simulation, powerful analysis and accurate prediction of complex biological processes. In this paper we have presented the basic components of such a combination: 1) Model checking-based parameter-space partitioning, for efficient and principled parameter selection;

2) Parallel simulation algorithms; and 3) Parallel curvature analysis algorithms, of the frames generated through simulation or optical mapping. Our algorithms take advantage of the NVIDIA's graphical processor cards Tesla and Fermi, and the associated CUDA architecture. Our results show a 444.444 speed-up of isopotential reconstruction compared to Matlab based contour algorithm. Our case studies identified promising signatures, of various forms of cardiac disorders, which may be used to predict their onset. We are currently working to parallelize the rest of our spiral-waves-classification algorithm (SCA) and to expand the variety of our case studies.

#### ACKNOWLEDGMENT

This research was performed under the NSF Expeditions project on Computational Modeling and Analysis for Complex Systems (CMACS) funded by the grant: NSF CCF-0926190. <http://cmacs.cs.cmu.edu>

#### 9. REFERENCES

- [1] D. Barkley. A model for fast computer simulation of waves in excitable media. *Physica*, 49(D):61–70, August 1991.
- [2] G. Beeler and H. Reuter. Reconstruction of the action potential of ventricular myocardial fibres. *Journal of Physiology*, 268(1):177–210, June 1977.
- [3] C. Belta and L. C. Havets. Controlling a class of non-linear systems on rectangles. *IEEE Transactions on Automatic Control*, 51(11):1749–1759, November 2006.
- [4] A. Bueno-Orovio, M. E. Cherry, and F. H. Fenton. Minimal model for human ventricular action potentials in tissue. *J. of Theor. Biology*, 253(3):544–560, 2008.
- [5] E. M. Cherry and F. H. Fenton. A tale of two dogs: Analyzing two models of canine ventricular electrophysiology. *American Journal of Physiology - Heart and Circulatory Physiology*, 292:H43–H55, 2007.
- [6] E. M. Cherry and F. H. Fenton. Visualization of spiral and scroll waves in simulated and experimental cardiac tissue. *New Journal of Physics*, 10:125016, 2008.
- [7] V. G. Fast and A. Kléber. Role of wavefront curvature in propagation of cardiac impulse. *journal of cardiovascular research*, 33(2):258–271, February 1997.
- [8] F. H. Fenton and E. M. Cherry. Models of cardiac cell. *Scholarpedia*, 3:1868, 2008.
- [9] R. Grosu, G. Batt, F. Fenton, J. Glimm, C. L. Guernic, S. Smolka, and E. Bartocci. From cardiac cells to genetic regulatory networks. In *Proc. of CAV'11, the 23rd International Conference on Computer Aided Verification*, LNCS, Cliff Lodge, Snowbird, Utah, USA, July 2011. Springer.
- [10] V. Iyer, R. Mazhari, and R. L. Winslow. A computational model of the human leftventricular epicardial myocytes. *Biophysical Journal*, 87(3):1507–1525, 2004.
- [11] D. Jones, R. Adams, and et al. Heart disease and stroke statistics 2010 update: A report from the american heart association. *Circulation*, December 2009.
- [12] M. Kay and R. Gray. Measuring curvature and velocity vector fields for waves of cardiac excitation in 2-d media. *IEEE Transactions on Biomedical Engineering*, 52(1):50–63, January 2005.
- [13] D. M. Khan. Cubic bezier least square fitting. *Matlab File Exchange*, July 2009.
- [14] A. Kléber. The fibrillating atrial myocardium. what can the detection of wave breaks tell us? *journal of cardiovascular research*, 48(2):181–184, August 2000.
- [15] C. H. Luo and Y. Rudy. A dynamic model of the cardiac ventricular action potential. I. Simulations of ionic currents and concentration changes. *Circulation Research*, 74(6):1071–1096, June 1994.
- [16] Mathworks. Matlab symbolic math toolbox, 1986. <http://www.mathworks.com/products/symbolic/>.
- [17] Matlab. Central's isocontour algorithm., 1986. <http://www.mathworks.com/matlabcentral/fileexchange/30525-isocontour>.
- [18] C. J. Myers. *Engineering Genetic Circuits*. CRC Press, 2010.
- [19] L. Priebe and D. J. Beuckelmann. Simulation study of cellular electric properties in heart failure. *Circulation Research*, 82:1206–1223, 1998.
- [20] D. F. Rogers and J. A. Adams. *Mathematical Elements of Computer Graphics*. McGraw-Hill Science/Engineering/Math, New York, 1989.
- [21] K. H. Ten Tusscher, D. Noble, P. J. Noble, and A. V. Panfilov. A model for human ventricular tissue. *American Journal of Physiology*, 286:H1573–H1589, 2004.